

PAPER

Room temperature synthesis of $\text{HfO}_2/\text{HfO}_x$ heterostructures by ion-implantation

To cite this article: Sanjoy Kumar Nandi *et al* 2018 *Nanotechnology* **29** 425601

View the [article online](#) for updates and enhancements.

Related content

- [Enhancement of resistive switching properties in \$\text{Al}_2\text{O}_3\$ bilayer-based atomic switches: multilevel resistive switching](#)
Sujaya Kumar Vishwanath, Hyunsuk Woo and Sanghun Jeon
- [Review of radiation effects on ReRAM devices and technology](#)
Yago Gonzalez-Velo, Hugh J Barnaby and Michael N Kozicki
- [Ion beam synthesis of indium-oxide nanocrystals for improvement of Oxide Resistive Random-Access Memories](#)
C Bonafos, G Benassayag, R Cours et al.



IOP | ebooks™

Bringing you innovative digital publishing with leading voices to create your essential collection of books in STEM research.

Start exploring the collection - download the first chapter of every title for free.

Room temperature synthesis of $\text{HfO}_2/\text{HfO}_x$ heterostructures by ion-implantation

Sanjoy Kumar Nandi^{1,2} , Dinesh Kumar Venkatachalam¹, Simon Ruffell³, Jonathan England³, Pedro Luis Grande^{1,4} , Maarten Vos¹  and Robert Glen Elliman¹

¹ Department of Electronic Materials Engineering, Research School of Physics & Engineering, The Australian National University, Canberra, ACT 2601, Australia

² Department of Physics, University of Chittagong, Chittagong-4331, Bangladesh

³ Varian Semiconductor Equipment, Silicon Systems Group, Applied Materials Inc., United States of America

⁴ Instituto de Física, Universidade Federal do Rio Grande do Sul, Porto Alegre, RS, Brazil

E-mail: Rob.Elliman@anu.edu.au

Received 7 May 2018, revised 23 July 2018

Accepted for publication 1 August 2018

Published 15 August 2018



CrossMark

Abstract

Implantation of Hf films with oxygen ions is shown to be an effective means of fabricating high-quality $\text{HfO}_2/\text{HfO}_x$ heterostructures at room temperature, with the layer composition and thicknesses determined by the ion energy and fluence. Implantation with 3 keV O^+ ions to a fluence of 1×10^{17} ions cm^{-2} produces a polycrystalline (monoclinic-) HfO_2 layer extending from the surface to a depth of ~ 12 nm, and an underlying graded HfO_x layer extending an additional ~ 7 nm, while implantation with 6 keV O to a similar fluence produces a near-stoichiometric surface layer of 7 nm thickness and a graded substoichiometric layer extending to depth of ~ 30 nm. These structures are shown to be broadly consistent with oxygen range data but more detailed comparison with dynamic Monte Carlo simulations suggests that the near-surface region contains more oxygen than expected from collisional processes alone. The bandgap and dielectric strength of the HfO_2 layer produced by 3 keV; 1×10^{17} ions cm^{-2} implant is shown to be indistinguishable from those of an amorphous film deposited by atomic layer deposition at 200 °C. The utility of these layers is demonstrated by studying the resistive switching properties of metal-oxide-metal test structures fabricated by depositing a top metal contact on the implanted film. These results demonstrate the suitability of ion-implantation for the synthesis of functional oxide layers at room temperature.

Supplementary material for this article is available [online](#)

Keywords: ion-implantation, HfO_2 , heterostructures, non-volatile memory

(Some figures may appear in colour only in the online journal)

1. Introduction

Oxide films are generally used as passive insulating layers in modern microelectronic devices but are of increasing interest as the active material in a new generation of low-power nanoionic devices [1]. These exploit characteristic resistance changes caused by the drift and diffusion of mobile ions in the oxide layer and are of particular interest for applications such as: resistive random-access memory (ReRAM) as a replacement for non-volatile flash

memory; field-programmable gate arrays for reconfigurable electronics; and artificial synapses and neurons for neuromorphic computing nanoionic devices [2]. A wide range of techniques are used to fabricate the functional oxide films, including thermal oxidation, thermal and plasma-enhanced atomic layer deposition (ALD), non-reactive and reactive sputter deposition, and thermal and plasma-enhanced chemical vapor deposition [3–5]. Because nanoionic devices rely on mobile ions and exploit the properties of substoichiometric films, device fabrication is normally limited

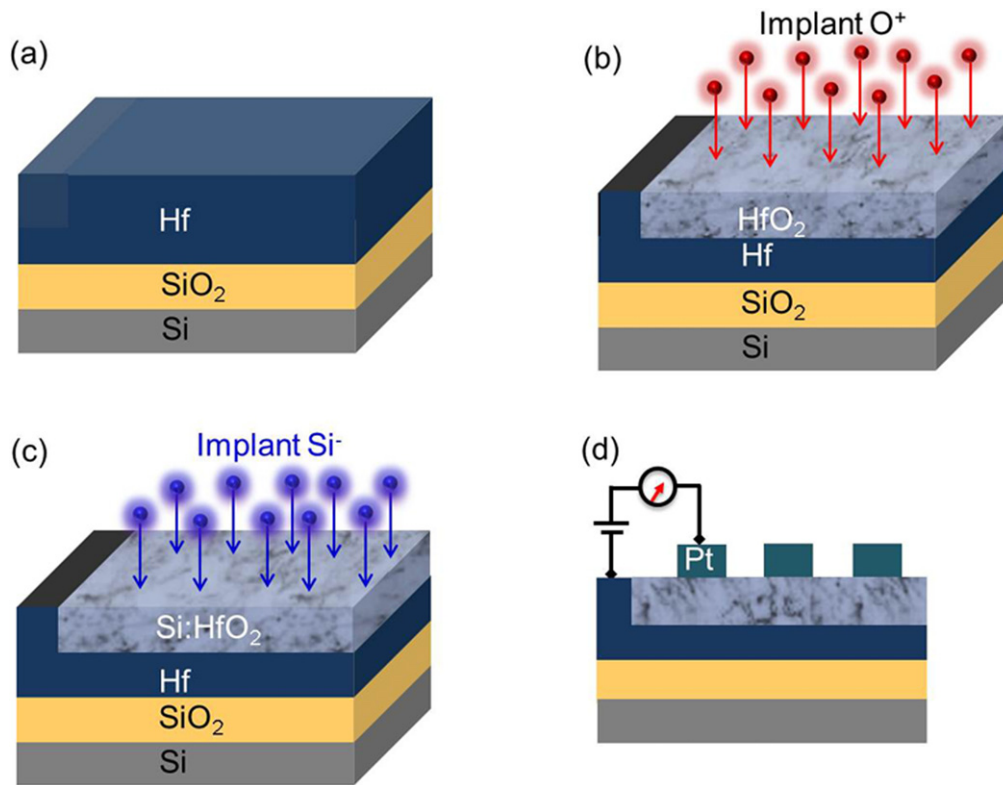


Figure 1. Schematic showing the test structure fabrication steps: (a) 50 nm Hf layer on thermally oxidized silicon wafer; (b) O implantation of the 50 nm Hf layer with a masking strip; (c) optional ion-implantation with 5 keV Si⁻ ions of different fluences (5×10^{13} , 1×10^{14} , 5×10^{15} , and 1×10^{15} ions cm⁻²) and (d) final metal-insulator-metal test structure after evaporation of top Pt contact pads.

to back-end of line processing where processing temperatures are limited to $<450^\circ\text{C}$. As a consequence there is particular interest in the development of low-temperature oxide synthesis methods [6].

Resistive switching in binary transition-metal oxides is typically mediated by the drift and diffusion of oxygen vacancies created by an initial soft-breakdown (forming) process [7–11]. The forming process can be difficult to control in stoichiometric films due to their low initial vacancy concentration and the large conductivity change during dielectric breakdown. The use of oxide/suboxide heterostructures mitigates the need for vacancy generation and generally leads to improved device performance, reliability and endurance [12, 13]. This can be achieved by direct deposition of oxide/suboxide films using techniques such as reactive sputter deposition, or by employed a reactive metal (e.g. Ti, Hf, Ta) to reduce part of a stoichiometric film [12].

Ion-implantation offers an alternative means of fabricating functional oxide films for resistive switching applications as it provides a controlled means of adjusting the film stoichiometry, and naturally produces a graded composition profile suited to the fabrication of oxide/suboxide heterostructures. It has previously been shown to produce CuO_x [14], and TaO_x [15–18] films suitable for resistive switching applications. Recent studies have also shown that doping can be used to modify the formation energy of oxygen vacancies and improve resistive switching reliability and uniformity

[19–21]. Such doping can be achieved through the co-deposition of the oxide and dopant, but again ion-implantation offers an attractive alternative approach [22, 23].

HfO₂ is currently employed as a high-*k* gate dielectric in CMOS devices and has been shown to exhibit excellent ReRAM characteristics. This study investigates the structure and properties of ion-beam synthesized HfO₂/HfO_x (oxide/suboxide) heterostructures produced by low-energy oxygen implantation into metallic Hf films. The functionality of the films is verified by testing their resistive switching characteristics.

2. Experimental details

Metal-insulator-metal test structures were fabricated on thermally oxidized Si wafers using the steps outlined in figure 1. First, a 50 nm Hf layer was deposited at room temperature over the full area of a wafer by DC sputter deposition from a Hf target (figure 1(a)). This was subsequently masked in selected regions and implanted with 3 keV O⁺ ions to fluences up to 1×10^{17} ions cm⁻² (figure 1(b)). The backside of the wafer was cooled during implantation to maintain the sample near room temperature. Smaller samples were cleaved from the full-wafer for subsequent processing and testing. Half of each sample was maintained in its as-implanted state (hereafter referred to as-implanted) while the other half was subsequently

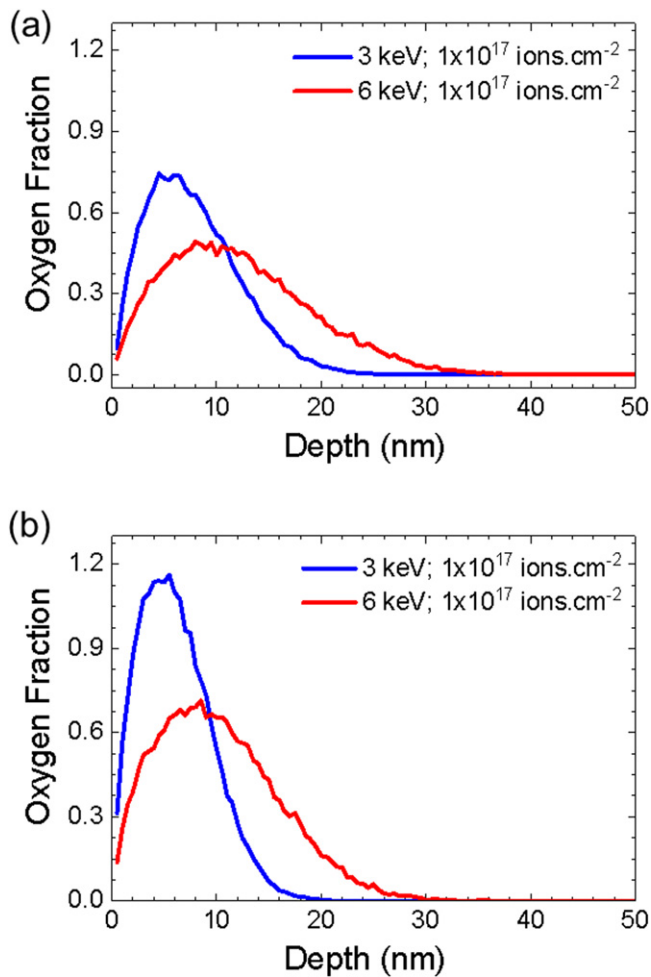


Figure 2. Ion range distributions for 3 keV O^+ ions and 6 keV O^+ ions implanted into (a) Hf and (b) HfO_2 , as calculated using the SRIM code [26]. The oxygen fraction in the latter refers to the implanted oxygen only.

implanted with 5 keV Si^- ions to fluences in the range from 5×10^{13} ions cm^{-2} to 1×10^{15} cm^{-2} (hereafter referred to Si-doped) (figure 1(c)). The implantation masks were then removed to provide access to unimplanted regions of the Hf film that extended beneath the implanted layer (figure 1(d)). A Pt film was finally e-beam evaporated through a shadow mask to define circular top contact pads of 100–250 μm diameters and complete the Pt/ HfO_x /Hf test structures (figure 1(d)). For comparison, similar Pt/Hf/ HfO_2 /Pt test structures were fabricated from 10 nm thick HfO_2 films deposited by ALD. In this case substrates were held at 200 °C during HfO_2 deposition, with the layer grown using alternating pulses of pure tetrakis (dymethylamido)-hafnium ($Hf(NMe_2)_4$) and H_2O vapor, with N_2 purged in the reaction chamber between pulses.

As-implanted films were studied by transmission electron microscopy (TEM), glancing incidence x-ray diffraction (GIXRD), electron Rutherford backscattering spectrometry (e-RBS) [24], reflection electron energy loss spectroscopy (REELS) and x-ray photoelectron spectroscopy (XPS). Electrical characterization was performed using a semiconductor parametric analyzer (Agilent B1500A).

3. Results and discussion

3.1. Implantation profiles

Figure 2 shows the oxygen range distributions for 3 keV and 6 keV O^+ ions implanted into Hf and HfO_2 , as calculated by the SRIM code (2013) [25, 26]. While this code does not include dynamic effects such as sputtering, diffusion or compositional changes, it can be used to estimate critical range parameters. Specifically, the simulations show that 3 keV oxygen ions implanted into Hf have a mean project range of 7.8 nm, with 4.5 nm straggling. In comparison, 3 keV oxygen ions implanted into HfO_2 have a mean projected range of 5.9 nm, with straggling of ~ 3.4 nm, reflecting the reduced ion range in HfO_2 due to its higher atomic density. As the composition of the surface layer is expected to evolve from Hf to HfO_2 during implantation, the actual range parameters will fall between these two extremes and if the profiles were unmodified by sputtering and diffusion this would give a peak O concentration of $\sim 7.4 \times 10^6$ ion $cm^{-3} \cdot \varphi$, where φ is the ion fluence in ions cm^{-2} . Given that the oxygen concentration in HfO_2 is 5.54×10^{22} ions cm^{-3} this would imply a critical fluence for HfO_2 synthesis of $\sim 7.5 \times 10^{16}$ $O cm^{-2}$. Similar analysis for the 6 keV implants shows that the O range in Hf is ~ 12 nm with straggling of ~ 7 nm, and in HfO_2 the range is ~ 10 nm with straggling of ~ 6 nm. In this case the critical fluence for oxide synthesis is $\sim 1.4 \times 10^{17}$ ions cm^{-2} . Although simplistic, these estimates are broadly consistent with experimental results which show that for 3 keV O implants a fluence of 5×10^{16} $O cm^{-2}$ fails to create a stoichiometric oxide layer (see supplementary information, which is available online at stacks.iop.org/NANO/29/425601/mmedia) while a fluence of 1×10^{17} ions cm^{-2} creates a HfO_2 layer of ~ 10 – 12 nm thickness, as discussed below.

3.2. Physical characterization

Figure 3 shows bright-field TEM images of Hf films after implantation with 3 keV O ions to a fluence of 1×10^{17} ions cm^{-2} (figure 3(a)) and after implantation with 6 keV O ions to a fluence of 1×10^{17} ions cm^{-2} (figure 3(b)). These show that the lower energy implant produces a well-defined surface layer of ~ 12 nm thickness, while the higher energy implant produces a thinner surface layer (~ 7 nm) and an underling ‘disordered’ layer of ~ 10 nm thickness. The higher resolution images further show that the near-surface layers are polycrystalline and have a structure consistent with monoclinic HfO_2 (determined from Fourier transform analysis of lattice images). These layer thicknesses are broadly consistent with the ion range data shown in figure 2 but it is interesting that they are polycrystalline, despite the high oxygen implant fluence. This contrasts with the case of O-implanted Ta which has been shown to produce amorphous Ta_2O_5 layers [27, 28].

Compositional depth profiling of the films was performed by XPS analysis, with results shown in figure 4(a). These data show a clear difference between the sample implanted with 3 keV O^+ to a fluence of 1×10^{17} ions cm^2 and other samples, with the former having a clear near-surface layer with O-concentration close to that of stoichiometric HfO_2

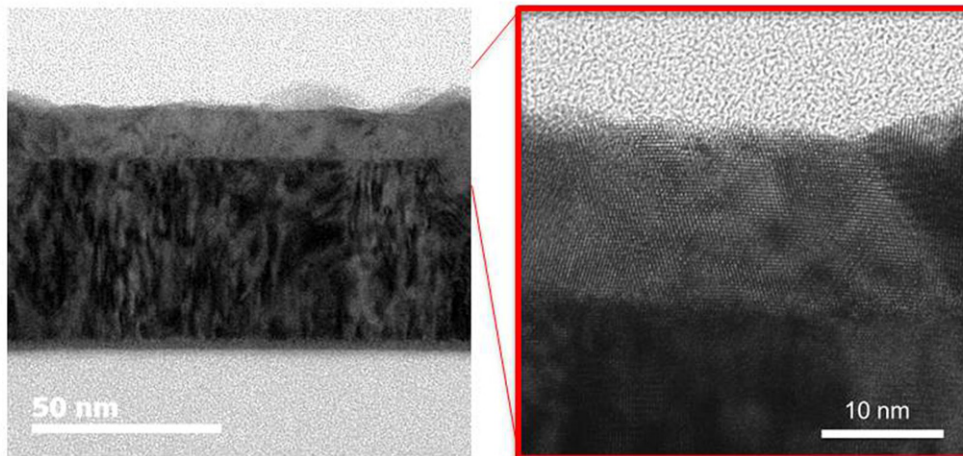
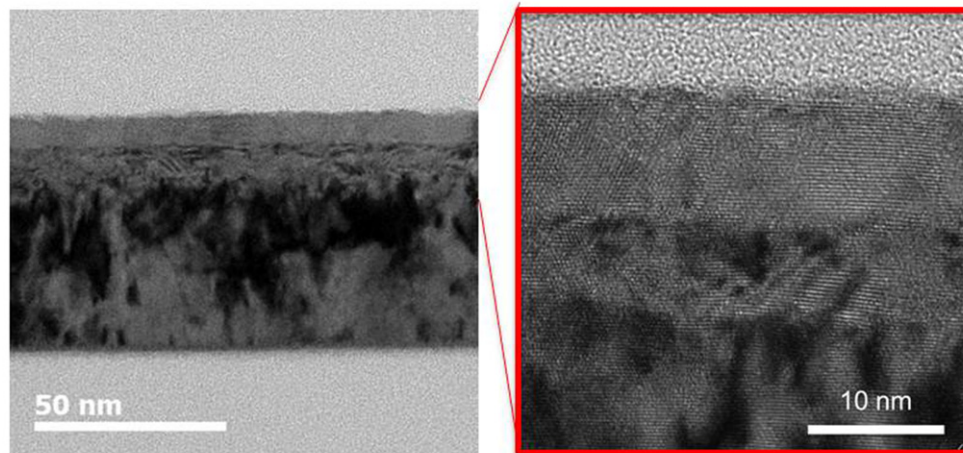
(a) 3 keV; 1×10^{17} ions.cm⁻²(b) 6 keV; 1×10^{17} ions.cm⁻²

Figure 3. Bright-field TEM images of (a) sample implanted with 3 keV O ions to a fluence of 1×10^{17} ions cm⁻², and (b) sample implanted with 6 keV O ions to a fluence of 1×10^{17} ions cm⁻².

extending from the surface to a depth of ~ 12 nm and the others having thin O-rich surface layers that are largely independent of the implant conditions. These results are consistent with the TEM analysis and range data and show that the oxygen concentration saturates at the stoichiometric composition of HfO₂ for the 3 keV; 1×10^{17} ions cm⁻² implant. This implies that excess oxygen (i.e. that in excess of the concentration required to form stoichiometric HfO₂) is either lost from the sample through redistribution to the surface, or extends the oxide thickness by diffusing to the HfO₂/HfO_x interface and reacting with Hf. We note that the thin oxygen-rich layers observed for other samples partly reflects the expected ~ 3 nm native oxide that forms on Hf metal when exposed to air [29].

GIXRD analysis of the oxide layer produced by the 3 keV; 1×10^{17} ions cm⁻² implant, shown in figure 4(b), confirms the polycrystalline nature of the film and shows that the dominant phase is monoclinic HfO₂. In contrast, the GIXRD spectrum

from an ALD HfO₂ film deposited at 200 °C exhibits a broad peak centered at 2θ values of 32°, consistent with amorphous HfO₂.

To confirm the stoichiometry of the surface layer and assess its electronic structure, implanted films were further characterized by electron Rutherford backscattering spectrometry (e-RBS) [30] and REELS. Figure 5(a) shows e-RBS spectra of the as-implanted sample for two different scattering geometries: normal incidence (perpendicular in) where elastic scattering includes contributions from the HfO₂ layer and underlying HfO_x and Hf layers, and rotated by 35° (glancing out) where elastic scattering is dominated by scattering from the HfO₂ layer. The elastic scattering peaks from Hf and O are clearly resolved (the recoil energy transferred from the projectile-electron to the nucleus depends on the atom's mass), with the O/Hf area ratio being larger for the glancing-out geometry (i.e. the O concentration is larger near the surface). A comparison of the peak ratios and scattering cross-sections

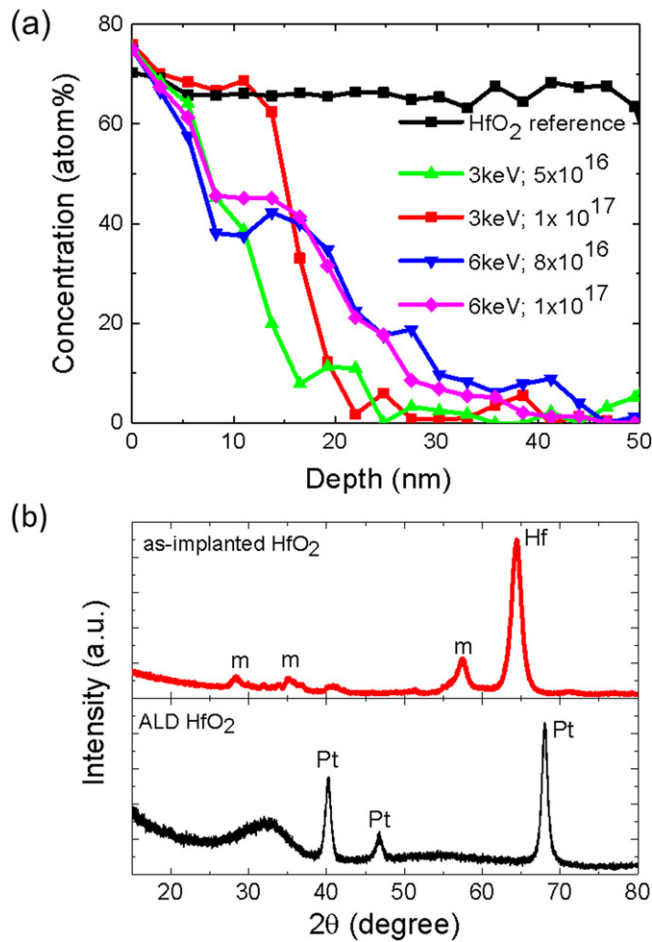


Figure 4. (a) XPS depth profiles of oxygen in implanted samples and (b) GIXRD spectrum of the as-implanted 3 keV; 1×10^{17} ions cm^{-2} sample and 10 nm ALD HfO₂ on Pt.

(NIST electron elastic-scattering cross-section database [31–33]) for the different scattering geometries confirmed the nominal stoichiometry of the surface layer to be HfO₂, with a thickness of ~12 nm. Unfortunately, the O peak is not background free and the variation in the background curves for different choices of stoichiometry results in a ~10% uncertainty of the O nominal stoichiometry.

Figure 5(b) shows corresponding REELS spectra from the as-implanted HfO_x sample and an ALD grown HfO₂ film performed with 5 keV electrons. For this energy the elastic scattering peaks from O and Hf cannot be resolved and their energy is taken as zero energy loss. The increase in scattering yield for energy losses greater than ~6.0 eV corresponds to elastically scattered electrons that have additionally undergone inelastic scattering, with the onset value corresponding to excitation of electrons across the oxide bandgap [30, 34–36]. For HfO₂ layers grown by ALD this gives a bandgap between 5.3 and 5.7 eV, depending on the assumptions made about the functional dependence of the onset [37]. For the O-implanted sample the onset is very similar, but there is increased yield at energy losses between 1 and 4 eV. This is attributed to Hf atoms that are not in a 4+ charge state, with the excess intensity arising from excitation of the remaining 5d electron, consistent with the film containing under-coordinated Hf.

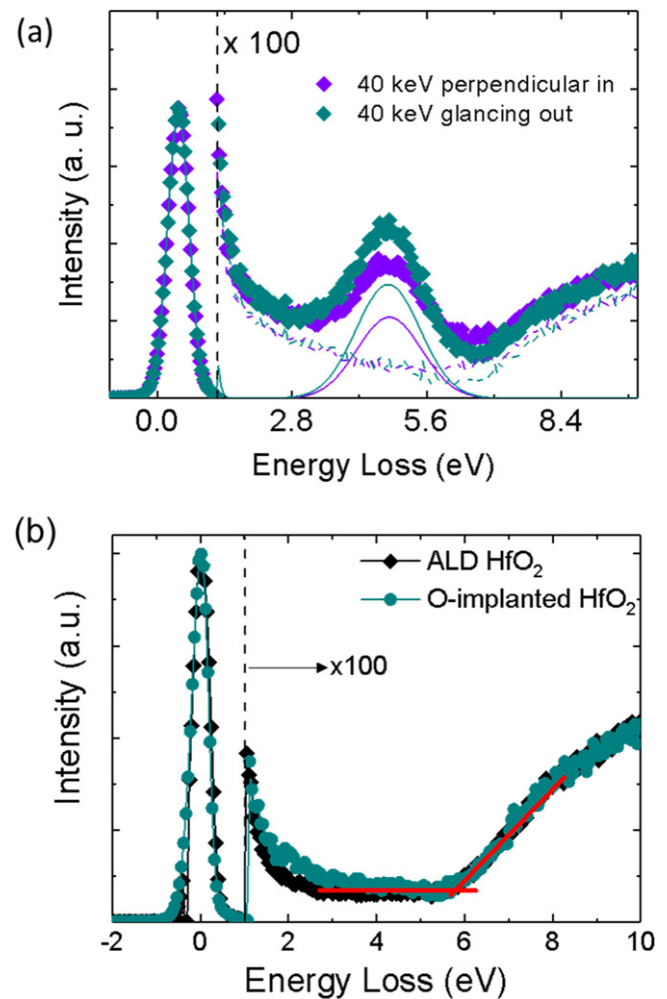


Figure 5. (a) e-RBS spectra of as-implanted 3 keV; 1×10^{17} ions cm^{-2} sample for two different geometries using 40 keV electrons, and (b) REELS spectra of the 3 keV; 1×10^{17} ions cm^{-2} and ALD samples using 5 keV electrons.

3.3. Dynamic profile simulations

To better understand the evolution of the oxide layer during ion implantation as well as the relative contributions of ion-implantation and sputtering to layer formation dynamic Monte Carlo simulations were undertaken using the TriDyn code [38, 39]. This code takes account of the changing composition of the sample during implantation and allows for oxygen in excess of the stoichiometric concentration to redistribute to regions of sub-stoichiometry. Results from these simulations are compared with TEM images and XPS profiles in figure 6.

Comparison of the TriDyn simulations and the XPS profiles shows that simulated profiles fail to reproduce the near-surface oxygen concentrations observed experimentally. This is particularly evident for the 6 keV; 1×10^{17} ions cm^{-2} implant where the simulation accurately reproduces the deeper implant profile but clearly underestimates the oxygen concentration in the thinner oxygen-rich surface layer. Interestingly this surface layer increases in thickness as the implant fluence increases as evidenced by an increase in the dielectric

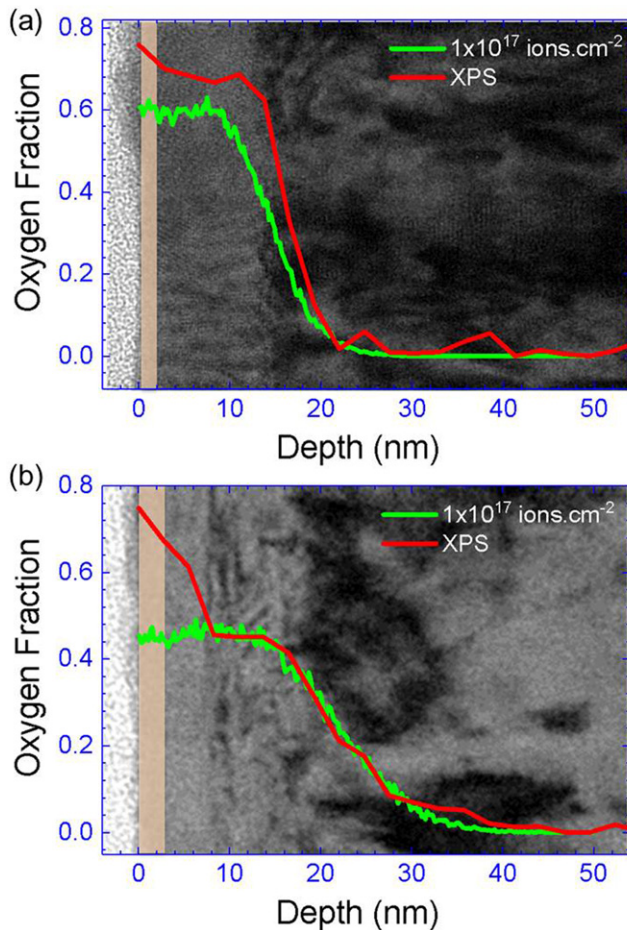


Figure 6. Bright-field TEM images, XPS profiles (red) and TriDyn simulated oxygen profiles (green) for a sample implanted with 3 keV O ions to a fluence of 1×10^{17} ions cm^{-2} , and (b) a sample implanted with 6 keV O ions to a fluence of 1×10^{17} ions cm^{-2} . Simulations assumed the presence of a 3 nm native oxide as indicated by the rectangular shaded area.

breakdown voltage. It is well known that radiation-enhanced diffusion and chemically-driven diffusion can enhance the transport of implanted ions to a growing compound or alloy layer to make it thicker but this would deplete oxygen at depths beyond the surface layer. The agreement between simulated and measured oxygen profiles for the 6 keV implant (figure 6(b)) suggests that this is not a significant effect in the present case. Attempts to model the excess surface oxygen by increasing the surface binding energies of Hf and/or O (i.e. reducing the sputtering yield) also failed to reproduce the experimental results suggesting that the excess surface oxygen comes from other sources. Possible sources include recoiled implantation of residual oxygen gas in the implant chamber or enhanced oxidation of the surface on exposure to atmosphere [40, 41].

3.4. Electrical properties

The electrical properties of the films were determined by measuring their electroforming and bipolar resistive switching

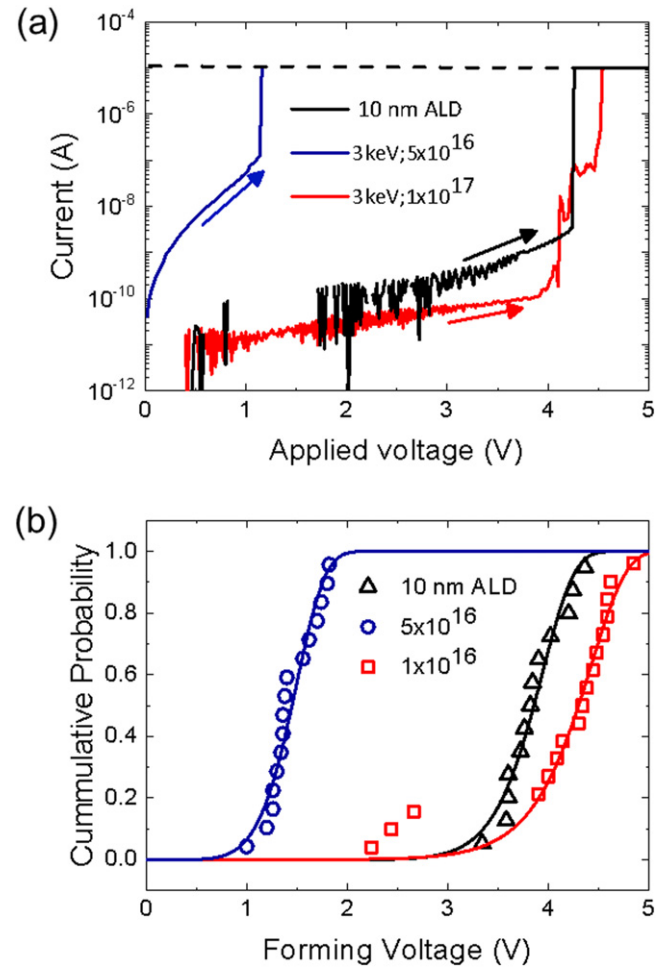


Figure 7. (a) The forming characteristics of the fabricated Pt/HfO₂/HfO_x/Hf ReRAM structure. (b) Weibull distribution of corresponding as-implanted and ALD Hf/HfO_x/HfO₂/Pt devices. Note that forming characteristics of implanted samples were measured with negative bias applied to the top electrode unless otherwise stated.

characteristics. The forming process is a one-off operation that is used to create a filamentary conduction path through the insulating layer. It corresponds to soft dielectric breakdown and is a direct measure of the film quality, with more defective or sub-stoichiometric films exhibiting higher leakage currents and lower forming (breakdown) voltages. To avoid permanent damage to the films, a 10 k Ω load resistor was placed in series with the test device and voltage scans were programmed to stop when the current reached a compliance limit of 10 μA . The polarity of the voltage ramp was consistent with that required for a ReRAM set operation; i.e. negative potential applied to the top (Pt) contact to induce oxygen vacancy migration from the deeper suboxide layer at the HfO₂/Hf interface towards the Pt layer. Figure 7(a) shows typical forming characteristics of as-implanted samples, as well as for a 10 nm ALD HfO₂ film in a structure of the form Pt/Hf/HfO₂/Pt. Weibull distributions for the measured forming voltages are summarized in figure 7(b). A mean breakdown voltage of ~ 4.3 V is measured for the 3 keV; 1×10^{17} ions cm^{-2} sample, and 3.8 V for the ALD film. This corresponds

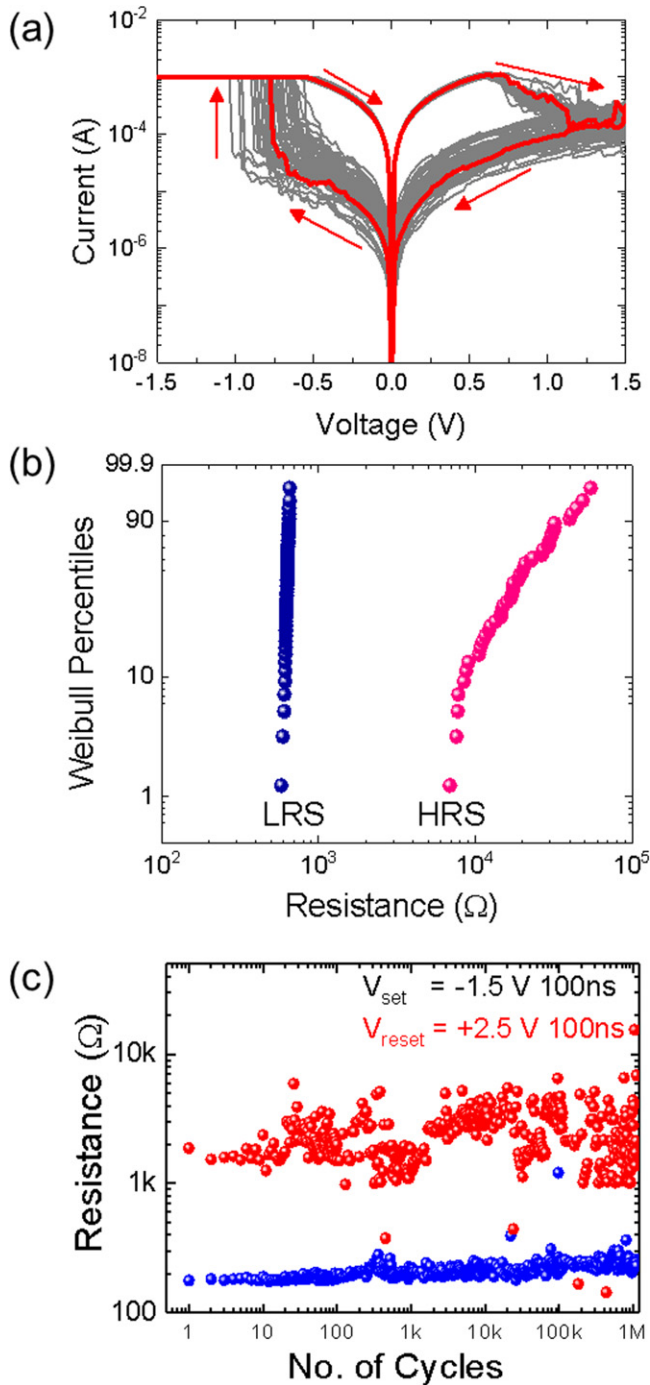


Figure 8. (a) Bipolar resistive switching characteristics for the 3 keV; 1×10^{17} ions cm^{-2} sample using a 1 mA set compliance current, (b) Weibull plot of the low (R_{LRS}) and high (R_{HRS}) resistance states and (c) pulse endurance characteristics.

to a breakdown field of $\sim 3.6 \text{ MV cm}^{-1}$ for the former and 3.8 MV cm^{-1} for the latter, confirming the excellent dielectric strength of the ion-beam synthesized film. This breakdown field strength is consistent with previous studies [10, 42–44]. Also included for comparison is the forming response of a sample implanted with 3 keV O^+ ions to a fluence of 5×10^{16} ions cm^{-2} . In this case breakdown occurs at 1 V, consistent with the presence of a native oxide of $\sim 2.6 \text{ nm}$ thickness.

Once formed, devices can be switched from low to high resistance states (RESET) and from high to low resistance states (SET) by applying positive and negative biases, respectively. Figure 8(a) shows typical bipolar resistive switching characteristics of the as-implanted 3 keV; 1×10^{17} O cm^{-2} sample for voltage scans over the range from -1.5 to 1.5 V. The characteristics are typical of HfO_2 devices, with an abrupt SET at ~ -0.7 V and a gradual RESET beginning at $\sim +0.7$ V. The resistance distributions of the low (LRS) and high (HRS) resistance states are plotted for 100 consecutive cycles in figure 8(b) and show a resistance window of ~ 10 . The observed spread in R_{HRS} is typical of HfO_2 RRAM devices and limits their reliability. Cycle-to-cycle stability and reproducibility of the devices was tested by subjecting the devices to electrical endurance tests in pulse mode using 100 ns pulses with $V_{\text{set}} = -1.5$ V, and $V_{\text{reset}} = +2.5$ V as shown in figure 8(c). These measurements demonstrate an endurance over 10^6 RS cycles while maintaining a memory window of ~ 10 . The effect of Si-doping on resistive switching characteristics was also explored as part of this study and shown to improve the switching characteristics (see supplementary information).

4. Conclusions

In conclusion, we have demonstrated ion-beam synthesis of high-quality $\text{HfO}_2/\text{HfO}_x$ heterostructures at room temperature by implanting O^+ ions into Hf films. Heterostructures synthesized by implantation with 3 keV O ions to a fluence of 1×10^{17} ions cm^{-2} were comprised of a polycrystalline (monoclinic) HfO_2 surface layer of ~ 12 nm thickness and an underlying graded substoichiometric layer of ~ 7 nm thickness. Samples implanted with 6 keV O ions to a fluence of 1×10^{17} ions cm^{-2} were predicted to be substoichiometric but exhibited a thin (~ 7 nm) oxygen-rich surface layer that increased in thickness with increasing fluence. In both cases the oxygen content of the near-surface region exceeded that predicted by dynamic Monte Carlo simulations suggesting that this surface layer may result from an additional source of oxygen such as recoil-implanted residual oxygen gas in the implant chamber.

The bandgap and a dielectric strength of the films produced by the 3 keV; 1×10^{17} ions cm^{-2} implant was found to be indistinguishable from that of amorphous HfO_2 films deposited by ALD at 200°C . The functionality of these films was demonstrated by measuring the resistive switching characteristics of simple metal–oxide–metal device structures that exploited the underlying Hf film as a bottom electrode and the graded HfO_x interface layer as an oxygen-exchange layer. The switching characteristics, reliability and endurance of these devices were found to be similar to those reported for HfO_2 films deposited by ALD at 200°C . A supplementary study further demonstrated that the resistive switching properties of these films could be improved by Si-doping, consistent with previous reports for ALD films.

Acknowledgments

The authors acknowledge financial support from the Australian Research Council (ARC) Discovery and Linkage programs, and from Varian Semiconductor Equipment (VSE), Applied Materials. We would also like to acknowledge NCRIS (Australian Facility for Advanced Ion-Implantation Research (AFAiIR)) and the ACT node of the Australian National Fabrication Facility (ANFF) for access to their research equipment and expertise. PLG would like to thank the Brazilian agencies CAPES, CNPq and FAPERGS for partially supporting this research project.

ORCID iDs

Sanjoy Kumar Nandi  <https://orcid.org/0000-0003-3453-074X>

Pedro Luis Grande  <https://orcid.org/0000-0003-0199-0520>

Maarten Vos  <https://orcid.org/0000-0003-2668-9216>

References

- [1] Akinaga H and Shima H 2010 Resistive random access memory (ReRAM) based on metal oxides *Proc. IEEE* **98** 2237–51
- [2] Fackenthal R *et al* 2014 19.7A 16 Gb ReRAM with 200 MB s⁻¹ write and 1GB s⁻¹ read in 27 nm technology 2014 *IEEE Int. Solid-State Circuits Conf. Digest of Technical Papers (ISSCC)* pp 338–9
- [3] Ritala M and Leskelä M 2002 Atomic layer deposition *Handbook of Thin Films* (Amsterdam: Elsevier) pp 103–59
- [4] Archer N 1979 Chemical vapour deposition *Phys. Technol.* **10** 152
- [5] Musil J, Baroch P, Vlček J, Nam K and Han J 2005 Reactive magnetron sputtering of thin films: present status and trends *Thin Solid Films* **475** 208–18
- [6] Yang J, Gill J, Kennedy J, Wang S-Q, Forester L and Ross M 1998 Electron beam processing for spin-on polymers and its applications to back-end-of-line (BEOL) integration *MRS Online Proc. Library Archive* **511** 49–55
- [7] Waser R and Aono M 2007 Nanoionics-based resistive switching memories *Nat. Mater.* **6** 833–40
- [8] Ha S D and Ramanathan S 2011 Adaptive oxide electronics: a review *J. Appl. Phys.* **110** 071101
- [9] Robertson J 2006 High dielectric constant gate oxides for metal oxide Si transistors *Rep. Prog. Phys.* **69** 327
- [10] Nandi S K, Liu X, Venkatachalam D K and Elliman R G 2015 Effect of electrode roughness on electroforming in HfO₂ and defect-induced moderation of electric-field enhancement *Phys. Rev. Appl.* **4** 064010
- [11] Nandi S, Llewellyn D, Belay K, Venkatachalam D, Liu X and Elliman R 2014 Effect of microstructure on dielectric breakdown in amorphous HfO₂ films *Microsc. Microanal.* **20** 1984–5
- [12] Chen Y Y *et al* 2013 Endurance/retention trade-off on HfO₂/metal cap 1T1R bipolar RRAM *IEEE Trans. Electron Devices* **60** 1114–21
- [13] Nandi S K, Liu X, Li S, Venkatachalam D K, Belay K and Elliman R G 2014 Resistive switching behavior in HfO₂ with Nb as an oxygen exchange layer 2014 *Conf. on Optoelectronic and Microelectronic Materials and Devices (COMMAD)* pp 290–3
- [14] Bishop S M, Bakhr H, Novak S W, Briggs B D, Matyi R J and Cady N C 2011 Ion implantation synthesized copper oxide-based resistive memory devices *Appl. Phys. Lett.* **99** 202102
- [15] Lee C B *et al* 2011 Highly uniform switching of tantalum embedded amorphous oxide using self-compliance bipolar resistive switching *IEEE Electron Device Lett.* **32** 399–401
- [16] Bishop S M, Briggs B D, Rice P Z, Capulong J O, Bakhr H and Cady N C 2013 Ion implantation synthesis and conduction of tantalum oxide resistive memory layers *J. Vac. Sci. Technol. B* **31** 012203
- [17] Ruffell S, Kurunzi P, England J, Erokhin Y, Hautala J and Elliman R G 2013 Formation and characterization of Ta₂O₅/TaO_x films formed by O ion implantation *Nucl. Instrum. Methods Phys. Res. B* **307** 491–4
- [18] Elliman R G *et al* 2013 Application of ion-implantation for improved non-volatile resistive random access memory (ReRAM) *Nucl. Instrum. Methods Phys. Res. B* **307** 98–101
- [19] Zhang H *et al* 2010 Ionic doping effect in ZrO₂ resistive switching memory *Appl. Phys. Lett.* **96** 123502
- [20] Zhao L, Park S-G, Magyari-Köpe B and Nishi Y 2013 Dopant selection rules for desired electronic structure and vacancy formation characteristics of TiO₂ resistive memory *Appl. Phys. Lett.* **102** 083506
- [21] Zhang H *et al* 2011 Gd-doping effect on performance of HfO₂ based resistive switching memory devices using implantation approach *Appl. Phys. Lett.* **98** 042105
- [22] Xie H *et al* 2012 Resistive switching properties of HfO₂-based ReRAM with implanted Si/Al ions *AIP Conf. Proc.* **1496** 26–9
- [23] Lin C Y *et al* 2007 Effect of top electrode material on resistive switching properties of ZrO₂ film memory devices *IEEE Electron Device Lett.* **28** 366–8
- [24] Marmitt G G, Rosa L F S, Nandi S K and Vos M 2015 Analysis of multi-layer ERBS spectra *J. Electron Spectrosc. Relat. Phenom.* **202** 26–32
- [25] Möller W, Eckstein W and Biersack J 1988 Tridyn-binary collision simulation of atomic collisions and dynamic composition changes in solids *Comput. Phys. Commun.* **51** 355–68
- [26] Pavlović M and Strašić I 2007 Supporting routines for the SRIM code *Nucl. Instrum. Methods Phys. Res. B* **257** 601–4
- [27] Elliman R *et al* 2013 Application of ion-implantation for improved non-volatile resistive random access memory (ReRAM) *Nucl. Instrum. Methods Phys. Res. B* **307** 98–101
- [28] Ruffell S, Kurunzi P, England J, Erokhin Y, Hautala J and Elliman R 2013 Formation and characterization of Ta₂O₅/TaO_x films formed by O ion implantation *Nucl. Instrum. Methods Phys. Res. B* **307** 491–4
- [29] Morant C, Galan L and Sanz J M 1990 An XPS study of the initial stages of oxidation of hafnium *Surf. Interface Anal.* **16** 304–8
- [30] Vos M, Grande P L, Nandi S K, Venkatachalam D K and Elliman R 2013 A high-energy electron scattering study of the electronic structure and elemental composition of O-implanted Ta films used for the fabrication of memristor devices *J. Appl. Phys.* **114** 073508
- [31] Grande P L, Vos M, Venkatachalam D K, Nandi S K and Elliman R G 2013 Determination of thickness and composition of high-*k* dielectrics using high-energy electrons *Appl. Phys. Lett.* **103** 071911
- [32] Salvat F, Jablonski A and Powell C J 2005 Elsepa—Dirac partial-wave calculation of elastic scattering of electrons and positrons by atoms, positive ions and molecules *Comput. Phys. Commun.* **165** 157–90
- [33] Powell C J, Jablonski A and Salvat F 2005 NIST databases with electron elastic-scattering cross sections, inelastic mean free paths, and effective attenuation lengths *Surf. Interface Anal.* **37** 1068–71

- [34] Vos M, Marmitt G G, Finkelstein Y and Moreh R 2015 Determining the band gap and mean kinetic energy of atoms from reflection electron energy loss spectra *J. Chem. Phys.* **143** 104203
- [35] Vos M, King S W and French B L 2016 Measurement of the band gap by reflection electron energy loss spectroscopy *J. Electron Spectrosc. Relat. Phenom.* **212** 74–80
- [36] Vos M, Liu X, Grande P L, Nandi S K, Venkatachalam D K and Elliman R G 2014 The use of electron Rutherford backscattering to characterize novel electronic materials as illustrated by a case study of sputter-deposited NbO_x films *Nucl. Instrum. Methods Phys. Res. B* **340** 58–62
- [37] Rafferty B and Brown L 1998 Direct and indirect transitions in the region of the band gap using electron-energy-loss spectroscopy *Phys. Rev. B* **58** 10326
- [38] Rosén D, Katardjiev I, Berg S and Möller W 2005 TRIDYN simulation of target poisoning in reactive sputtering *Nucl. Instrum. Methods Phys. Res. B* **228** 193–7
- [39] Möller W and Eckstein W 1984 Tridyn—a TRIM simulation code including dynamic composition changes *Nucl. Instrum. Methods Phys. Res. B* **2** 814–8
- [40] Magee T *et al* 1981 Recoil oxygen implants and thermal redistribution of oxygen in through-oxide arsenic-implanted Si *Appl. Phys. Lett.* **39** 564–6
- [41] Hirao T, Fuse G, Inoue K, Takayanagi S, Yaegashi Y and Ichikawa S 1979 The effects of the recoil-implanted oxygen in Si on the electrical activation of as after through-oxide implantation *J. Appl. Phys.* **50** 5251–6
- [42] Kukli K, Ritala M, Sajavaara T, Keinonen J and Leskelä M 2002 Atomic layer deposition of hafnium dioxide films from hafnium tetrakis (ethylmethanamide) and water *Chem. Vapor Depos.* **8** 199–204
- [43] Park H B *et al* 2003 Comparison of HfO₂ films grown by atomic layer deposition using HfCl₄ and H₂O or O₃ as the oxidant *J. Appl. Phys.* **94** 3641–7
- [44] Sokolov A S *et al* 2018 Influence of oxygen vacancies in ALD HfO_{2-x} thin films on non-volatile resistive switching phenomena with a Ti/HfO_{2-x}/Pt structure *Appl. Surf. Sci.* **434** 822–30